

热障涂层高温 TGO 生长变化

韩志勇, 王晓梅, 王志平

(中国民航大学 天津市民用航空器适航与维修重点实验室, 天津 300300)

摘 要: 通过 Abaqus 有限元分析软件对热障涂层在高温氧化过程中的热氧化物层(thermally growth oxide, TGO) 生长机制进行研究. 结果表明, 当高温氧化到 100 h 时, TGO 厚度由初始的 $0.5\ \mu\text{m}$ 生长至 $6.7\ \mu\text{m}$ 且在不同位置 TGO 的厚度略微不同. 随着高温时间的增加, 热障涂层在 TGO 的波峰、波谷以及涂层边界处容易出现应力较大值, 且和周围材料相比应力明显较大. 此时, 这些位置容易达到材料开裂临界应力, 形成裂纹萌生点, 使得涂层失效. 在高温氧化过程中, 涂层吸收总能量为 $43.6\ \text{J}$, 其中少部分转化为涂层变形所消耗的能量, 剩下的能量为高温氧化过程中涂层成分改变、微观组织改变以及裂纹萌生扩展提供能量.

关键词: 热障涂层; 热氧化物; Abaqus 有限元软件

中图分类号: TG 172.6 **文献标识码:** A **文章编号:** 0253-360X(2014)11-0005-04

0 序 言

热障涂层是将耐高温、抗腐蚀、高隔热的陶瓷材料通过物理或化学方法沉积在基体合金表面, 以提高基体合金抗高温氧化腐蚀能力, 降低合金表面工作温度^[1-4]. 对于等离子喷涂的热障涂层, 影响涂层热循环寿命的因素包括^[5-9]: 表面陶瓷层与金属基底之间的热膨胀不匹配、陶瓷层发生相变、黏结层发生氧化和腐蚀、金属基底的粗糙度以及陶瓷层的烧结等. 热障涂层最主要的失效原因为 TGO 的生成^[10, 11]. 热生长氧化物层厚度增长会产生微缺陷, 其在低界面粗糙度的情况下产生的影响尤为明显. 氧化过程中, TGO 经历平面内压缩变形, 其压缩变形程度在冷却过程中增强. 变形强度和相应的应变能密度被自身的伸长和平面外的位移变形减弱, 导致陶瓷涂层屈曲和粘结层的粘塑性变形, 产生垂直于涂层界面的拉应力及缺陷^[12].

刘文开^[13]对热障涂层高温氧化后发现陶瓷层和粘结层之间的氧化物生成主要分为三个阶段, 初期主要是 Al_2O_3 和其它元素的尖晶石氧化物共同存在; 稳定氧化阶段主要为 Al_2O_3 的选择性氧化; 复杂氧化阶段由于出现贫铝现象使得尖晶石数量增加. 韩玉君^[14]对热障涂层在 $1\ 000\ ^\circ\text{C}$ 高温下进行不同时间的烧结后发现, 长期的高温氧化使得热障涂层中的氧扩散由空穴扩散转变为“陶瓷层晶格氧扩散机

制”为主, 且在经过 122 h 后新形成的 TGO 氧化物也主要以 Al_2O_3 为主.

文中通过 Abaqus 有限元软件, 对高温氧化过程中的 TGO 生长进行初步模拟探索, 观察 TGO 生长以及生长过程对涂层应力分布、能量变化的影响, 从而帮助理解实际过程中 TGO 生长机制, 为热障涂层高温过程研究奠定理论基础.

1 热障涂层结构

1.1 涂层结构

现在应用最为广泛的为双层结构的热障涂层, 由陶瓷层(top coating, TC) 和粘结层(bond coating, BC) 组成. 文中陶瓷层($8\%\ \text{Y}_2\text{O}_3$ 的 ZrO_2 , 质量分数) 厚度为 $250\ \mu\text{m}$, 粘结层(Ni-22Cr-10Al-1Y) 厚度为 $100\ \mu\text{m}$ 以及初始 TGO(主要为 Al_2O_3) 厚度为 $0.5\ \mu\text{m}$. 由于涂层的厚度相对基体很小, 因此计算模型只取粘接层、TGO 层和陶瓷层, 如图 1 所示.

文中计算研究热障涂层在持续的高温氧化过程中 TGO 厚度变化以及高温氧化处理后涂层内的残余应力分布. 设定涂层初始为室温 $25\ ^\circ\text{C}$, 升温至 $1\ 000\ ^\circ\text{C}$, 高温氧化 $3.6 \times 10^5\ \text{s}$. 在整个计算过程中的涂层周围空间中的温度分布是均匀的. 计算过程中采用非线性计算, 因此重点考虑涂层材料的物性参数随温度场的变化^[10]. 忽略涂层制备过程产生的残余应力的影响以及此过程中的蠕变, 残余应力的分布与过程无关, 所以计算过程只考虑 $25\ ^\circ\text{C}$ 和 $1\ 000\ ^\circ\text{C}$ 这两个初末状态.



图 1 热障涂层结构

Fig. 1 Thermal barrier coatings schematic

1.2 模型设置

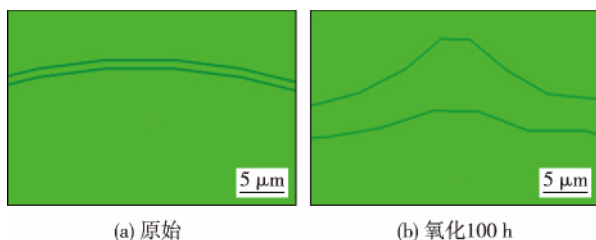
TGO 的初始形状为正弦曲线,波长为 $200\ \mu\text{m}$,幅值为 $40\ \mu\text{m}$ 。由于模拟的有限性以及界面的重复性,因此只选取一个正弦波,左右边界设定为对称,表示涂层在横向的延伸性。

由于涂层的厚度一般小于 $500\ \mu\text{m}$,所以相对于基体(几千微米)来说很小,因此模拟过程中涂层底层设置为完全固定,无任何方向的相对移动。由于模型网格划分尺寸和类型对计算结果都有一定的影响,因此通过查阅文献和预模拟结果,最后采用 C3D8R(三维 8 节点减缩积分)的单元类型,网格尺寸为 4。

2 结果与讨论

2.1 TGO 生长厚度变化

图 2 为不同厚度下的 TGO 示意图,可以很明显地看出,TGO 厚度从初始的 $0.5\ \mu\text{m}$ 增加至 $6.7\ \mu\text{m}$,且 TGO 不同位置生长的最终厚度略有差异,这是由 TGO 的形貌以及陶瓷层、粘结层和 TGO 自身在不同高温下变形所导致的。



(a) 原始

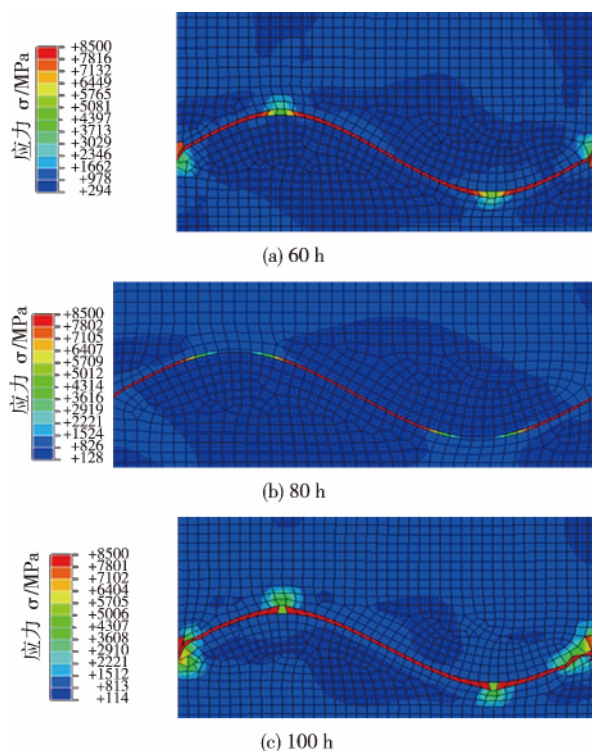
(b) 氧化 100 h

图 2 TGO 厚度云图

Fig. 2 Atlas of TGO at different time points

2.2 TGO 生长过程中应力变化

图 3 为不同时间下的模型应力-时间变化云图,可以很明显地看出,随着时间的增加,TGO 厚度逐渐增加,因此产生的变形量逐渐增加,导致陶瓷层、粘结层和 TGO 之间的不匹配开始逐渐增大。云图中 TGO 处应力快速增加,同时对 TGO 附近的陶瓷层和粘结层的影响也随之增大,TGO 周围的变形量也相应增加,因此图 3 中 TGO 边界、波峰以及波谷等应力容易堆积处表现为网格开始不容易收敛,产生畸形变化。



(a) 60 h

(b) 80 h

(c) 100 h

图 3 不同时间下应力沿着 TGO 路径的分布云图

Fig. 3 Atlas of stress distribution along TGO layer at different increments

图 4 和图 5 为波峰周围横向和纵向的应力分布。图 4~图 7 分别为涂层氧化 60、80、100、140 和 146 h 后应力分布曲线。 x 表示界面上各点与模型最左端的距离。通过对比可以看出,随着波峰距离的增加,左右两端应力均快速减小,均保持在 $1\ 000\ \text{MPa}$ 左右。而横向和纵向波峰处应力为最大,横向应力由 $3\ 000\ \text{MPa}$ 增加到 $8\ 400\ \text{MPa}$ 。波峰横向应力分布为以波峰为中心,左右对称形态,而波峰纵向应力分布的波峰左端为 TC 内应力分布,由于 TC 和 TGO 热物参数不同因而应力快速增加,最大应力变化率为 $1.37\ \text{MPa/s}$ 。而波峰右端为 BC 内应力变化趋势,应力在 BC 内快速减小,最大应力变化率为 $2.50\ \text{MPa/s}$ 。

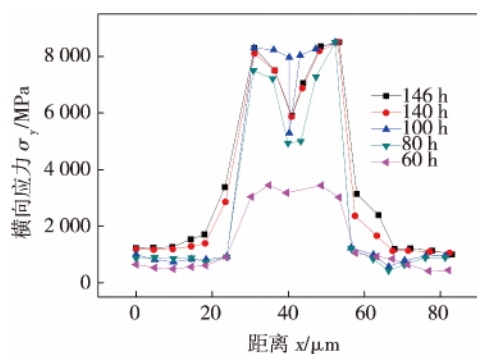


图 4 波峰处横向应力 - 距离分布

Fig. 4 Curve of horizontal stress and distance at peak

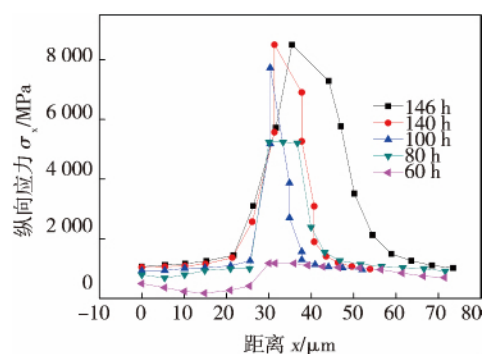


图 7 波谷处纵向应力 - 距离分布

Fig. 7 Curve of vertical stress distribution and distance at valley

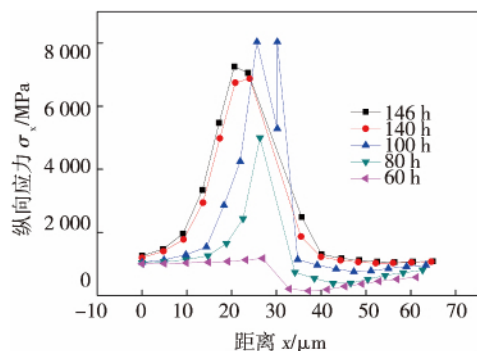


图 5 波峰处纵向上应力 - 距离分布

Fig. 5 Curve of vertical stress and distance at peak

图 6 和图 7 为波谷处的横向和纵向应力分布, 和波峰处的横向和纵向应力分布具有类似的趋势. 横向应力分布为左右对称, 而纵向应力为: TC 内变化较快, 应力变化率为 2.3 MPa/s, 而 BC 内应力变化和 TC 相比则率为较小, 应力变化率为 1.5 MPa/s, 应力变化量较为均匀.

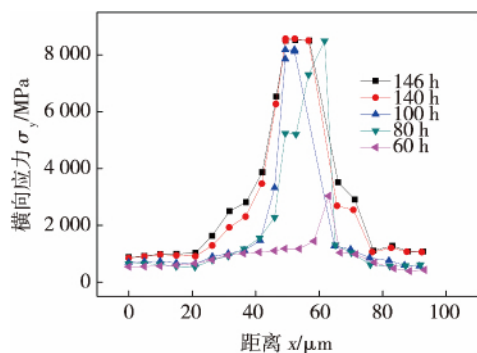


图 6 波谷处横向应力 - 距离分布

Fig. 6 Curve of horizontal stress distribution and distance at valley

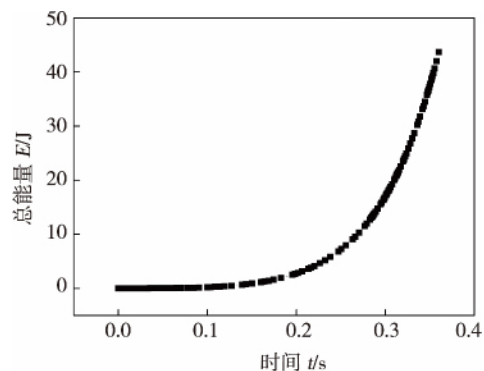


图 8 高温氧化过程中能量变化曲线

Fig. 8 Whole energy variation during high-temperature oxidation process

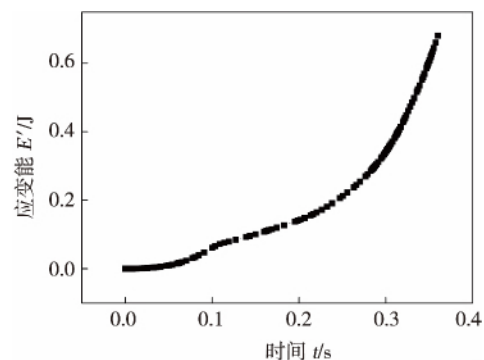


图 9 高温氧化过程应变能变化曲线

Fig. 9 Strain energy variation during high-temperature oxidation process

热障涂层进行高温氧化本身就是吸收能量的过程, 吸收的能量转化为涂层的变形能量以及实际过

应力的突变,从而为裂纹的产生提供有利条件.

3 结 论

(1) 随着氧化时间的增加,涂层的厚度呈现增加趋势,当氧化时间增加至 100 h 时,TGO 的厚度也从初始的 $0.5\ \mu\text{m}$ 增加至 $6.7\ \mu\text{m}$,且 TGO 不同位置的厚度略有差异.

(2) 随着 TGO 厚度的增加,涂层的应力分布也逐渐呈现出一定趋势,在涂层边界处、TGO 的波峰处以及波谷处应力和其它位置相比明显较大,更容易成为达到临界应力的位置,形成裂纹萌生点,从而成为材料失效的萌发点.

(3) TGO 的波峰与波谷处的横向应力和纵向应力变化趋势大致相同,都表现为随着波峰/波谷距离的增加,应力呈现减小趋势,当距离足够远时,涂层应力不容易受到 TGO 氧化过程的影响.

(4) 在高温氧化过程中,涂层的能量也呈现增加趋势,当氧化到 100 h 时,涂层吸收的总能量为 43.6 J,其中 0.68 J 的能量转化为涂层变形所消耗的能量,其它能量为高温氧化过程中涂层成分改变,为微观结构改变以及裂纹萌生扩展提供能量.

参考文献:

- [1] 管恒荣,李美姮,孙晓峰,等. 高温合金热障涂层的氧化和失效研究[J]. 金属学报,2002,38(11):1133-1140.
Guan Hengrong, Li Meiheng, Sun Xiaofeng, *et al.* Research on the oxidation and failure of high temperature alloy thermal barrier coatings[J]. Acta Metallurgica Sinica, 2002, 38(11): 1133-1140.
- [2] Miller R A. Oxidation-based model for thermal barrier coating life[J]. Journal of the American Ceramic Society, 1984, 67(8): 517-521.
- [3] Demasi-Marcin J T, Sheffler K D, Bose S. Mechanisms of degradation and failure in a plasma-deposited thermal barrier coating[J]. Journal of Engineering for Gas Turbines and Power, 1990, 112(4): 521-526.
- [4] Brindley W J, Miller R A. Thermal barrier coating life and isothermal oxidation of low-pressure plasma-sprayed bond coat alloys[J]. Surface and Coatings Technology, 1990, 43: 446-457.
- [5] Lee C H, Kim H K, Choi H S, *et al.* Phase transformation and bond coat oxidation behavior of plasma-sprayed zirconia thermal barrier coating[J]. Surface and Coatings Technology, 2000, 124(1): 1-12.
- [6] Mumm D R, Evans A G. On the role of imperfections in the failure of a thermal barrier coating made by electron beam deposition[J]. Acta Materialia, 2000, 48(8): 1815-1827.
- [7] Christensen R J, Lipkin D M, Clarke D R, *et al.* Nondestructive evaluation of the oxidation stresses through thermal barrier coatings using Cr^{3+} piezospectroscopy[J]. Applied Physics Letters, 1996, 69(24): 3754-3756.
- [8] Busso E P, Lin J, Sakurai S, *et al.* A mechanistic study of oxidation-induced degradation in a plasma-sprayed thermal barrier coating system: Part I: model formulation[J]. Acta Materialia, 2001, 49(9): 1515-1528.
- [9] Shillington E A G, Clarke D R. Spalling failure of a thermal barrier coating associated with aluminum depletion in the bond-coat[J]. Acta Materialia, 1999, 47(4): 1297-1305.
- [10] Chen W R, Wu X, Marple B R, *et al.* Oxidation and crack nucleation/growth in an air-plasma-sprayed thermal barrier coating with NiCrAlY bond coat[J]. Surface and Coatings Technology, 2005, 197(1): 109-115.
- [11] 韩志勇,张 华,王志平. TGO 界面特征对热障涂层残余应力的影响[J]. 焊接学报,2012,33(12):33-36.
Han Zhiyong, Zhang Hua, Wang Zhiping. Influence of TGO interface characteristics on the residual stress in thermal barrier coatings[J]. Transactions of the China Welding Institution, 2012, 33(12): 33-36.
- [12] Busso E P, Lin J, Sakurai S. A mechanistic study of oxidation-induced degradation in a plasma-sprayed thermal barrier coating system: Part II: Life prediction model[J]. Acta Materialia, 2001, 49(9): 1529-1536.
- [13] 刘文开. 提高 Al 在 TBCs 过渡层中扩散速率对 TBC 使用寿命影响的研究[D]. 河北工业大学,2008.
- [14] 韩玉君. 热障涂层高温氧化相变及失效分析[D]. 河北工业大学,2010.

作者简介: 韩志勇,男,1970 年出生,博士,教授,硕士生导师. 主要从事涂层材料制备与计算. 发表论文 10 余篇. Email: zyhan@cauc.edu.cn

MAIN TOPICS ABSTRACTS & KEY WORDS

Arc behavior of A-MIG welding and microstructure of aluminum alloy welded joint

LU Hao¹, XING Liwei¹, LIANG Zhimin² (1. Technique Headquarters, CSR Qingdao Sifang CO. LTD., Qingdao 266111, China; 2. Faculty of Material Science and Engineering, Hebei University of Science and Technology, Shijiazhuang 054300, China). pp 1 – 4

Abstract: A new welding method-activating flux MIG (A-MIG) welding was proposed in this paper, which can obtain welded joint with high quality and reduce lack of fusion. The arc morphology during this welding method were collected and analyzed. The results show that the current density in A-MIG welding was higher than that in conventional MIG welding. Based on the analysis with scanning electron microscope and transmission electron microscope, the inspection results by comparing A-MIG welding and conventional MIG welding show that the addition of activating flux did not affect precipitated phases and distribution of Mn, Cr and Ti alloying elements.

Key words: activating flux MIG welding; aluminum alloy; arc morphology; microstructure

TGO growth of high temperature thermal barrier coatings

HAN Zhiyong, WANG Xiaomei, WANG Zhiping (Tianjin Key Laboratory for Civil Aircraft Airworthiness and Maintenance, Civil Aviation University of China, Tianjin 300300, China). pp 5 – 8

Abstract: Growth mechanism of thermally growth oxide (TGO) in thermal barrier coatings (TBCs) was investigated by finite element analysis software ABAQUS. After high temperature oxidation for 100 hours, the thickness of TGO increased from 0.5 μm to 6.7 μm . With the increasing of high temperature oxidation, stresses in the peaks, valleys and interface of TGO were obviously larger than in other places. Meanwhile, cracks were prone to initiate and propagate at these locations, and eventually led to spalling of the entire coating. During high temperature oxidation, the total absorbed energy of coating was 43.6 J, some of which was consumed for coating deformation, and the remaining for changes of coating composition and microstructure, and crack propagation.

Key words: thermal barrier coating; thermally growth oxide; finite element software ABAQUS

Numerical simulation of temperature field in weaving welding based on ladder model

ZONG Xuemei, WU Bin, ZHANG Liping, LI Wen (Jiangsu Xuzhou Construction Research Institute, Xuzhou Construction Machinery Group, Xuzhou 221004, China). pp 9 – 12

Abstract: According to the characteristic of weaving welding, an arc swing ladder model was established on basis of strip heat source and numerical simulation of temperature field in

Q345 steel plate butt joint with weaving welding was done using commercial software SYSWELD. The transient temperature field and thermal cycle curves in the welded zone were obtained. The results showed that the transient temperature field with arc-weaving ladder model was different from that with strip heat source model, and the weld pool with ladder model was elliptical with small head and big rump when the heat source moved from the middle to both sides. The thermal cycle curves with ladder model were also different from those with strip heat source model, and they had a wave crest both in heating and cooling, which reflected that the weld was affected by the arc weaving upon heating and cooling.

Key words: weaving welding; ladder model; numerical simulation; temperature field

Effect of peak temperature and cooling rate in welding thermal cycle on microstructure and properties of CGHAZ in SA508-3 steel

LÜ Xiaochun^{1,2}, HE Peng¹, QIN Jian², DU Bing², HU Zhongquan³ (1. State Key Laboratory of Advanced Welding and Joining, Harbin Institute of Technology, Harbin 150001, China; 2. Harbin Welding Institute, Harbin 150028, China; 3. Department of Mechanical Engineering, Tsinghua University, Beijing 100084, China). pp 13 – 17

Abstract: Because the microhardness and absorbed energy change greatly after CGHAZ experiencing different peak temperature and cooling rate in welding thermal cycle, the CGHAZ in the SA508-3 steel joint is highly unstable. When the peak temperature in the second welding thermal cycle was 600 – 700 $^{\circ}\text{C}$, the CGHAZ could get a better match between hardness and toughness. The formation of hidden martensite near grain boundary and grain coarsening should be avoided after the CGHAZ experienced secondary welding thermal cycle which peak temperature was 750 – 950 $^{\circ}\text{C}$ and $t_{8/5}$ was 10 s.

Key words: SA508-3 steel; coarse grain heat-affected zone; peak temperature; cooling rate

Effect of pore on super long fatigue life of aluminium alloy welded joint

HE Chao, CUI Shiming, LIU Yongjie, WANG Qingyuan (Key Laboratory of Energy Engineering Safety and Disaster Mechanics, Ministry of Education, Sichuan University, Chengdu 610065, China). pp 18 – 22

Abstract: In order to investigate the fatigue behavior and failure mechanism in super long life regime, ultrasonic fatigue tests were performed on 5052 aluminium alloy welded joint. The results show that the fatigue strength of welded joint descended about 73.3% as compared to the base metal with the same fatigue life. Fatigue failure occurred in the very high cycle fatigue regime. Fatigue crack initiated from the welding defects (pores) from the observation of SEM. To clarify the effect of pores on the